



## Refractory high-entropy alloys

O.N. Senkov <sup>a,b,\*</sup>, G.B. Wilks <sup>a,c</sup>, D.B. Miracle <sup>a</sup>, C.P. Chuang <sup>d</sup>, P.K. Liaw <sup>d</sup>

<sup>a</sup> Air Force Research Laboratory, Materials and Manufacturing Directorate, Wright-Patterson Air Force Base, OH 45433, USA

<sup>b</sup> UES, Inc., 4401 Dayton-Xenia Rd., Dayton, OH 45432, USA

<sup>c</sup> General Dynamics, Corp., Dayton, OH 45431, USA

<sup>d</sup> Department of Material Science and Engineering, The University of Tennessee, Knoxville, TN 37996, USA

### ARTICLE INFO

#### Article history:

Received 20 April 2010

Received in revised form

26 May 2010

Accepted 31 May 2010

Available online 23 June 2010

#### Keywords:

B. Alloy design

B. Crystallography

C. Casting

D. Microstructure

F. Electron microscopy, scanning

### ABSTRACT

Two refractory high-entropy alloys with near-equiatomic concentrations, W–Nb–Mo–Ta and W–Nb–Mo–Ta–V, were produced by vacuum arc melting. Despite containing many constituents both alloys have a single-phase body-centered cubic (BCC) structure. The lattice parameters  $a = 3.2134(3)$  Å for the quaternary alloy and  $a = 3.1832(2)$  Å for the quinary alloy were determined with high-energy X-ray diffraction using a scattering vector length range from 0.7 to 20 Å<sup>-1</sup>. The alloy density and Vickers microhardness were  $\rho = 13.75$  g/cm<sup>3</sup> and  $H_V = 4455$  MPa for the W–Nb–Mo–Ta alloy and  $\rho = 12.36$  g/cm<sup>3</sup> and  $H_V = 5250$  MPa for the W–Nb–Mo–Ta–V alloy. The exceptional microhardness in these alloys is greater than any individual constituent, suggesting the operation of a solid-solution-like strengthening mechanism.

© 2010 Elsevier Ltd. All rights reserved.

## 1. Introduction

Metallic alloys with superior mechanical and functional properties remain in high demand for the aerospace industry. Conventional alloys, especially for structural applications, are sometimes considered a relatively mature technology. Typically, such alloys have a base element that dominates the chemistry, accounting for ~80% (by weight) or more of the total formulation. Even superalloys, with as many as 12 elements in a single alloy, often contain over 50% of the base element. Only in comparatively rare cases, have superalloys with roughly 20% each of up to three transition metal elements (Fe, Ni, Co, and/or Cr) been developed. This limited scope of alloying strategy mainly stems from the fact that ternary or higher-order intermetallic compounds form unexpectedly in multi-component alloys, generally after long-term exposure at elevated operating temperatures. These new phases often have complex crystal structures that do not support plasticity, and scavenge desirable elements from the host phase. Formation of these complex intermetallics typically heralds a reduction in mechanical properties, corrosion resistance, and microstructure stability. This long-held experience provides a strong disincentive for unnecessarily complex alloy formulations.

Within the past several years, a fundamentally new alloying concept has been proposed [1–4]. Termed high-entropy alloys (HEAs), these new materials are formed by combining  $n$  elements of roughly equimolar concentrations. When  $n$  is large (typically  $n \geq 5$ ), the high entropy of mixing can stabilize solid-solution-like phases with relatively simple crystal structures rather than forming the conventionally expected complex intermetallic phases. Thus, while these alloys may be compositionally complex, they are microstructurally simple. Clearly, this concept offers a vast opportunity to explore, discover, and develop fundamentally new classes of alloys for structural and functional applications. Alloying element combinations previously perceived as objectionable due to microstructure instability may now be a possibility, suggesting completely new families of light metal alloys, high strength metals, and high-temperature metals.

To date, high-entropy alloy research seems to emphasize alloys based on the late transition metals such as Fe, Ni, Co and Cu. To the authors' knowledge, there have been no systematic efforts to explore HEAs based primarily on refractory element constituents. Since metallic alloys for high-temperature load-bearing structures and thermal protection remain in high demand for the aerospace industry, there is a clear rationale for exploring HEAs composed of constituents with high melting temperatures. Therefore, this work describes the development and characterization of two obvious compositions of HEAs based on refractory elements. The first alloy was chosen to contain equal concentrations of W, Nb, Mo, and Ta,

\* Corresponding author. UES, Inc., 4401 Dayton-Xenia Rd., Dayton, OH 45432, USA. Tel.: +1 937 2551320.

E-mail address: oleg.senkov@wpafb.af.mil (O.N. Senkov).

while the second alloy was created by the addition of an equal atomic percent of V to the same constituents.

## 2. Experimental procedures

W–Nb–Mo–Ta and W–Nb–Mo–Ta–V alloys—referred to as Alloy 1 and Alloy 2, respectively—were prepared at Pittsburgh Materials Technology, Inc. (Jefferson Hills, PA) by vacuum arc melting of equimolar mixtures of the corresponding elements. High purity Ti was used as a getter for residual gases in the high vacuum chamber. W, Mo, and V were in the form of 45.7 mm diameter rods with a purity of 99.7%, 99.0%, and 99.9% (by weight), respectively, while Ta and Nb were in the form of chips and had a purity of 99.0% and 99.99%, respectively. The alloys were prepared in the form of buttons of ~10 mm thick and ~60–70 mm in diameter. To achieve a homogeneous distribution of elements in the alloys, the buttons were remelted four times, flipped for each melt, and had a total time of over 1 h in the liquid state. The buttons had lustrous surfaces indicating no oxidation occurred during vacuum arc melting. The final composition of the alloys, determined by inductively-coupled plasma-optical emission spectroscopy (ICP-OES), is reported in Table 1. It should be noted that the composition of each alloy is close to equiatomic. The microstructure and properties of the alloys were studied in the as-cast condition. The crystal structure was identified with the use of high-energy synchrotron X-ray diffraction (MAR345 Image Plate Detector, Advanced Photon Source, Argonne National Laboratory). The samples for X-ray diffraction were in the form of ~0.75 mm thick plates. The X-ray energy was 105 keV and the beam spot-size was  $0.05 \times 0.05$  mm. The scattering vector ranged from 0.7 to  $20 \text{ \AA}^{-1}$ .

The density of the alloys was measured with an AccuPyc 1330V1.03 pycnometer. The pycnometer cell volume was  $12.2284 \text{ cm}^3$ . The weight of the samples was from 10 to 15 g and was measured with an accuracy of  $\pm 0.0001$  g, while the volume of the samples was determined with an accuracy of  $\pm 0.0001 \text{ cm}^3$  by measuring the free volume of the loaded cell using He gas and ten purges.

Alloy microstructures were analyzed with the use of a scanning electron microscope (SEM) equipped with both backscatter electron (BSE) and energy dispersive spectroscopy (EDS) detectors. Electron probe micro-analysis (EPMA) was conducted using a Cameca SX100 micro-analyzer operating at an accelerating voltage of 15 keV. The effective excitation volume at the sample surface, from which the elemental composition was collected, was ~3  $\mu\text{m}$  in diameter and ~3  $\mu\text{m}$  deep. Vickers microhardness was measured on polished cross-section surfaces using a 136-degree Vickers diamond pyramid under 500 g load applied for 30 s.

## 3. Results and discussions

### 3.1. Crystal structure

X-ray diffraction patterns of the studied W–Nb–Mo–Ta and W–Nb–Mo–Ta–V alloys are reported in Fig. 1a and b, respectively. In these figures, the scattering vector length  $Q$  is plotted versus the scattered X-ray intensity. The inter-planar spacing  $d$  is related to  $Q$  by the relationship

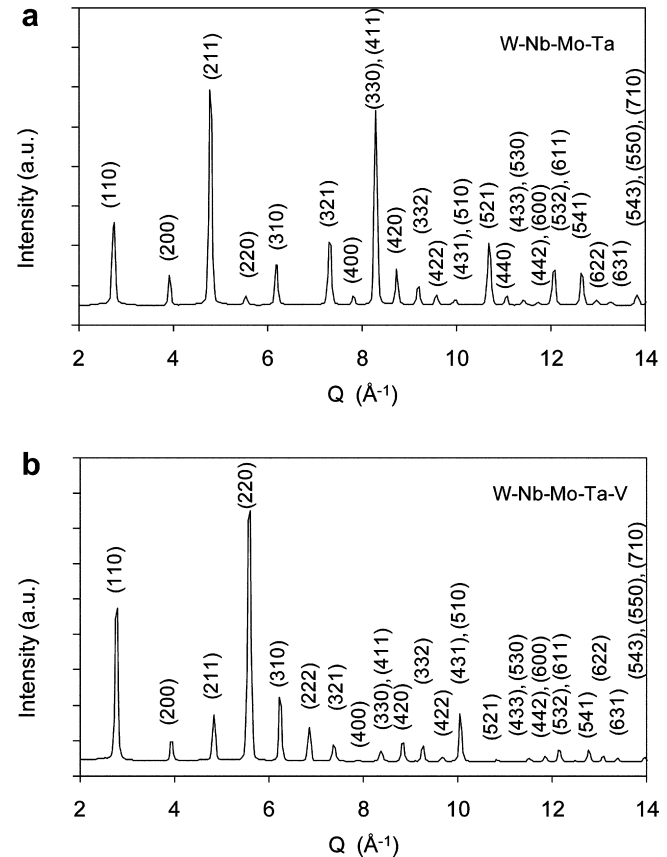


**Fig. 1.** X-ray diffraction patterns of the (a) W–Nb–Mo–Ta and (b) W–Nb–Mo–Ta–V alloys. All peaks in the patterns belong to the same BCC crystal lattice and their indexes are shown.

$$d = 2\pi/Q = \lambda/(2 \sin \Theta) \quad (1)$$

where  $\lambda$  is the wavelength of the incident x-rays and  $\Theta$  is half the scattering angle. All peaks on these X-ray patterns have been identified with appropriate indices and are congruent with a single BCC phase (Pearson symbol cI2). The large number of the X-ray peaks provided high accuracy in determining the lattice parameters, which were  $a_1 = 3.2134(3) \text{ \AA}$  for W–Nb–Mo–Ta (Alloy 1) and  $a_2 = 3.1832(2) \text{ \AA}$  for W–Nb–Mo–Ta–V (Alloy 2). The different relative intensities of the same peaks in the two alloys were most likely due to apparent texture effects caused by the small number of grains within the X-ray excited volume.

Formation of the BCC crystal structure in the two developmental alloys was expected, as all five elements used to produce these alloys have identical BCC crystal lattices. Moreover, these elements also have similar atomic radii (see Table 2) and similar valence numbers (6 for V, Nb and Ta and 5 for W and Mo) [5]. Following the Hume-Rothery rules, solid solutions are formed in binary systems of these metals over a whole range of the concentrations (although a  $\text{TaV}_2$  phase forms in the Ta–V system below  $1310^\circ\text{C}$ ) [6]. The lattice parameters of pure elements, taken from Ref. [7], are given in Table 2. Using the rule-of-mixtures approach, a ‘theoretical’ crystal lattice parameter,  $a_{\text{mix}}$ , of an alloy can be estimated:

$$a_{\text{mix}} = \sum c_i a_i \quad (2)$$

where  $c_i$  and  $a_i$  are the atomic fraction and the lattice parameter of element  $i$ . The calculated  $a_{\text{mix}}$  for the studied alloys are given in Table 2. The  $a$  values, determined by X-ray diffraction are also given in this table. Within experimental error, the lattice parameter of

**Table 1**

Chemical composition (in wt.%/at.%) of two refractory alloys produced by vacuum arc melting.

Alloy ID/element	W	Nb	Mo	Ta	V
Alloy 1	36.0/27.3	15.2/22.7	17.8/25.6	31.7/24.4	0.0/0.0
Alloy 2	33.0/21.1	16.2/20.6	17.6/21.7	23.9/15.6	9.08/21.0

**Table 2**

The crystal lattice parameter,  $a$ , density,  $\rho$ , and Vickers hardness,  $H_v$ , of high purity W, Nb, Mo, Ta and V metals, and two developmental alloys. The melting temperature,  $T_m$ , and atomic radius,  $r$ , of the pure metals and, calculated for the two alloys (Eq. (4)), are also given here.

Metal	W	Nb	Mo	Ta	V	Alloy 1 Calc	Alloy 1 Exp	Alloy 2 Calc	Alloy 2 Exp
$a, \text{\AA}$	3.158	3.301	3.1468	3.303	3.039	3.2230	3.2134	3.1827	3.1832
$\rho, \text{g/cm}^3$	19.25	8.57	10.28	16.65	6.11	13.64	13.75	12.36	12.36
$H_v, \text{MPa}$	3430	1320	1530	873	628	1841	4455	1596	5250
$T_m, ^\circ\text{K}$	3695	2750	2896	3290	2183	3177	—	2946	—
$r, \text{\AA}$	1.39	1.46	1.39	1.46	1.34	—	—	—	—

Alloy 2 follows the rule of mixtures. This may indicate that the BCC phase is a fully disordered solid solution. In contrast, the calculated lattice parameter of Alloy 1 is about 0.3% larger than the experimentally measured value, indicating that some solution ordering may be occurring. Solid solution ordering can also be responsible for the absence of peaks from the crystallographic planes (222), (800), (660), (822), (840), and (664) in Alloy 1 even though they are present in the X-ray diffraction pattern of Alloy 2.

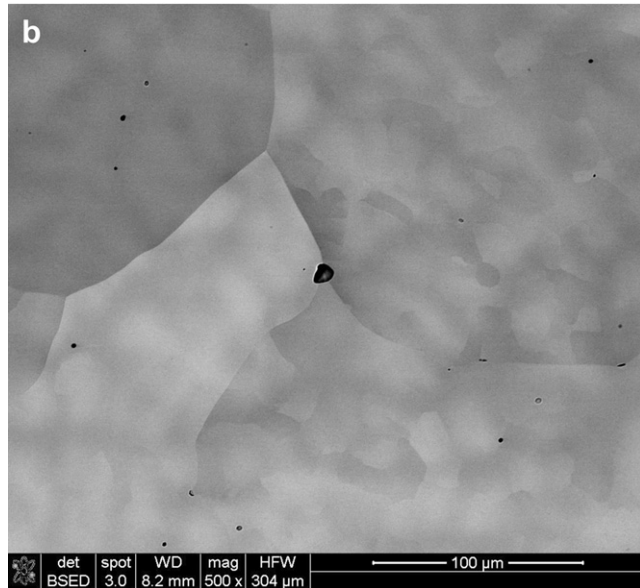
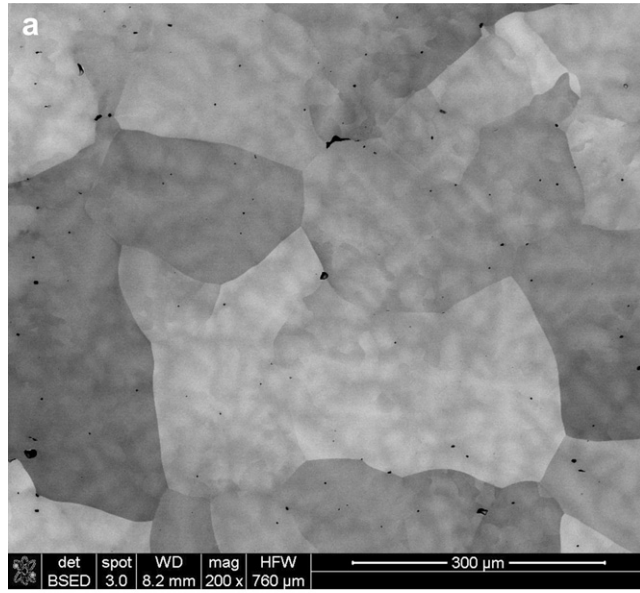


**Fig. 2.** SEM backscatter electron images of a polished cross-section of W–Nb–Mo–Ta alloy taken at two different magnifications.

### 3.2. Density

The densities of the alloys were determined to be  $\rho_1 = 13.75 \pm 0.03 \text{ g/cm}^3$  for the W–Nb–Mo–Ta alloy and  $\rho_2 = 12.36 \pm 0.01 \text{ g/cm}^3$  for the W–Nb–Mo–Ta–V alloy (see Table 2). These values can be compared with the theoretical density of a disordered solid solution,  $\rho_{\text{theor}}$ , as given by

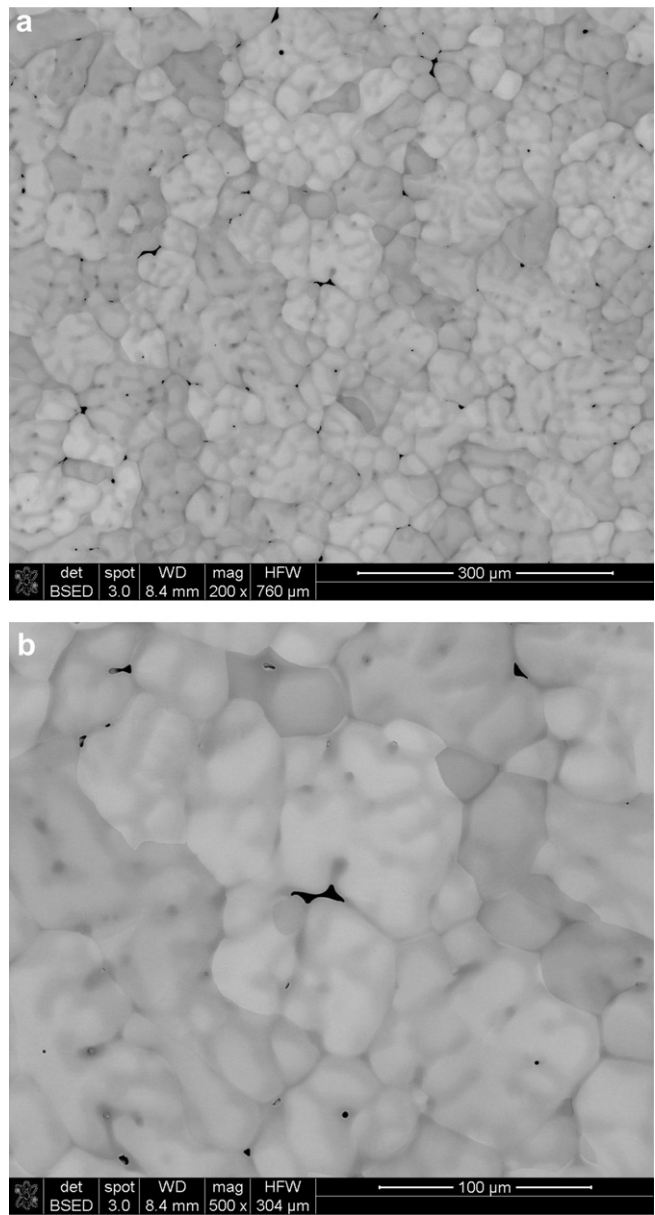


**Fig. 3.** SEM backscatter electron images of a polished cross-section of W–Nb–Mo–Ta–V alloy taken at two different magnifications.

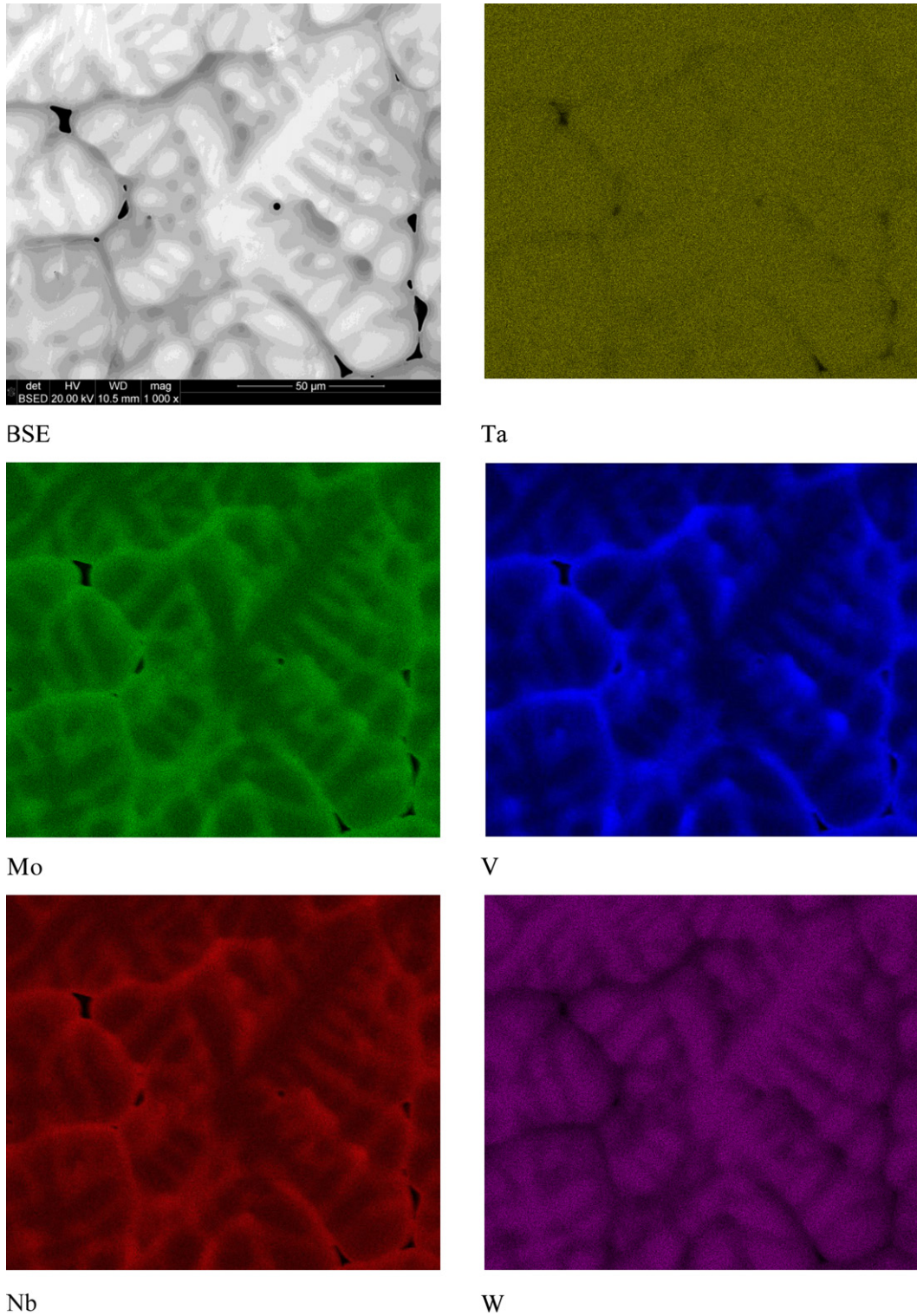


**Fig. 4.** Energy Dispersive Spectroscopy of the W–Nb–Mo–Ta–V alloy. The relative intensity of each element map gives a qualitative sense for the segregation characteristics of that constituent; Ta is uniformly distributed, while W solidifies in the dendrite cores, and Mo, V, and Nb segregate to the interdendritic region.

$$\rho_{\text{theor}} = \frac{\sum c_i A_i}{\sum \frac{c_i A_i}{\rho_i}} \quad (3)$$

where  $A_i$  and  $\rho_i$  are the atomic weight and density of element  $i$ . The  $\rho_i$  values of the constituents [5] and calculated  $\rho_{\text{theor}}$  values for the two alloys in this study are also reported in Table 2. It can be seen that the measured density of Alloy 1 is about 0.8% higher than theoretically

expected for a disordered solid solution, while that of Alloy 2 is identical to the corresponding calculated density. These density results agree with the results of the earlier X-ray analysis, which suggest that some solution ordering may be present in Alloy 1, while Alloy 2 seems to be a fully disordered solid solution despite the fact that the addition of V to the quaternary alloy encourages the formation of a compound with one of the other constituents ( $V_2Ta$ ) [6].

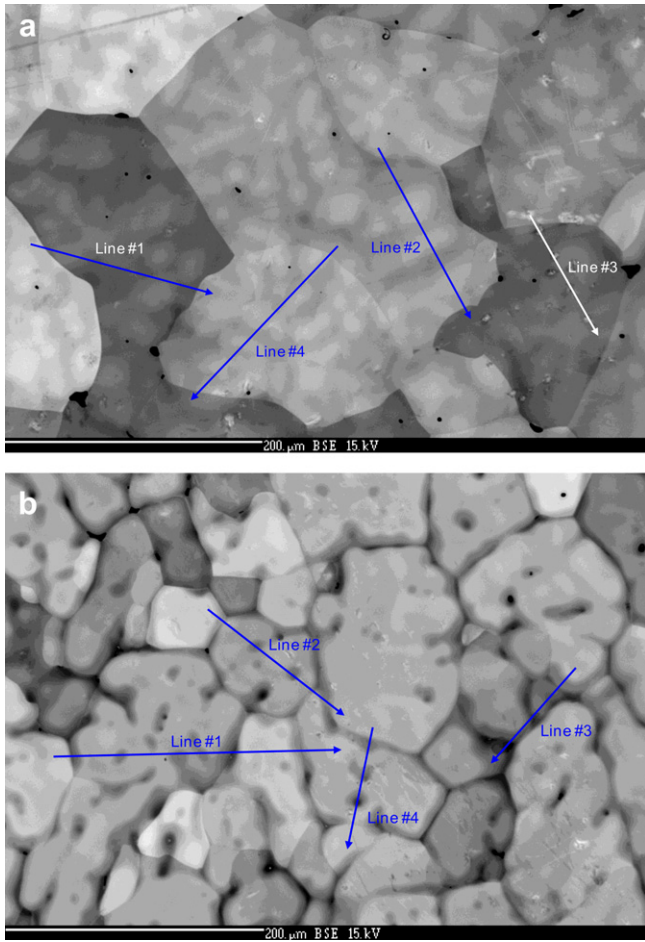


**Fig. 5.** SEM backscatter electron images of the regions of (a) Alloy 1 and (b) Alloy 2 from which the EPMA was conducted. The elemental composition gradients were determined along the drawn lines with the spacious resolution of 2  $\mu\text{m}$ .

### 3.3. Microstructure

SEM backscatter electron images of the refractory alloys are shown in Figs. 2 and 3. Large grains of about 200  $\mu\text{m}$  in diameter are observed in Alloy 1 (Fig. 2) while Alloy 2 has a much finer grain size, on the order of 80  $\mu\text{m}$  (Fig. 3). Intergranular and intra-granular pores can be seen in both alloys, however, their volume fraction is less than 5%. Recognizing the contribution of these pores, it is expected that our measured densities are slightly lower than would be expected in a fully dense manifestation of these materials. Uneven Z-contrast inside the grains indicates slightly different compositions of dendritic and interdendritic regions due to constitutional segregation during solidification. The lighter Z-contrast in both materials indicates that the dendrite arms are enriched with heavier elements than the interdendritic regions. From the EDS analysis of the quaternary alloy (Fig. 4), the qualitative segregation characteristics can be visualized: Ta is uniformly distributed, while presumably the asymmetry in melting temperature between constituents (see Table 2) encourages W to solidify first in the dendrite cores, ultimately forcing Mo, V, and Nb into the interdendritic region. The segregation of elements in Alloy 1, excluding V, was qualitatively similar to Alloy 2. The dendrite arm thickness was about the same in both alloys  $\sim 20\text{--}30 \mu\text{m}$ .

### 3.4. Electron probe micro-analysis

Electron probe micro-analysis (EPMA) was used to quantify the level of element segregation between the dendrite arms and interdendritic regions. For this analysis, elemental compositions were collected at different points along the lines drawn through grains and dendrites with a spatial separation of 2  $\mu\text{m}$ . Fig. 5 shows the sample regions used for the EPMA and Figs. 6 and 7 show concentrations of the constituent elements along the selected lines. In total, 542 points were analyzed for Alloy 1 and 512 points for Alloy 2. The average,  $C_{\text{aver}}$ , minimum,  $C_{\text{min}}$ , and maximum,  $C_{\text{max}}$ , concentrations of the elements determined by EPMA in these two alloys are given in Tables 3 and 4, respectively. The average

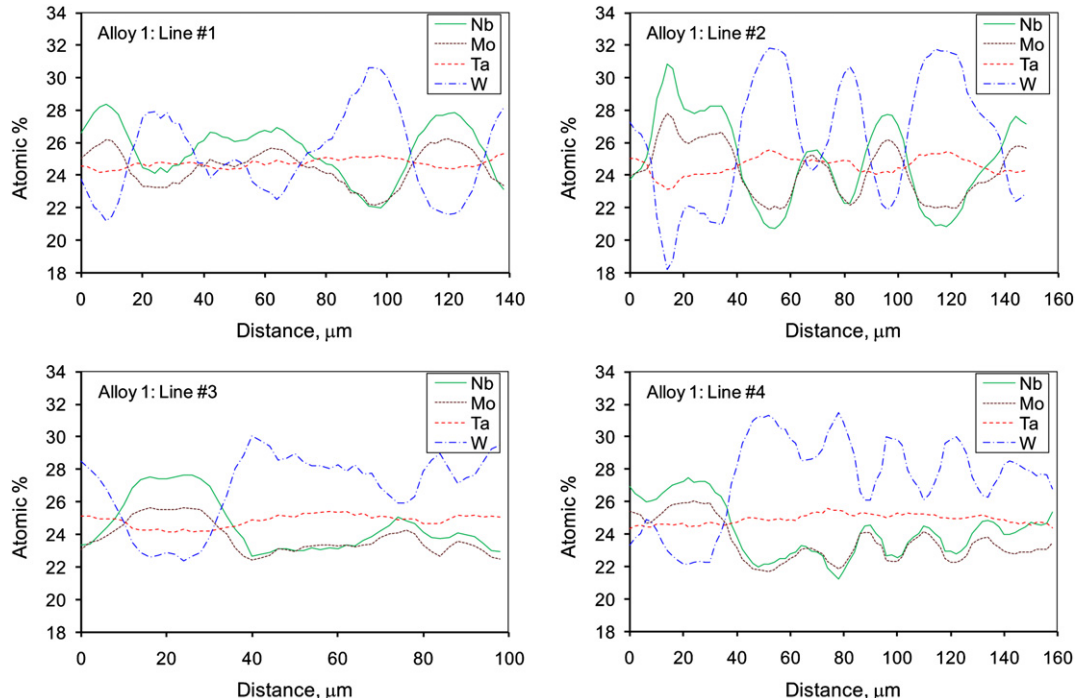


**Fig. 6.** Distribution of elements in Alloy 1 along the lines shown in Fig. 5a.

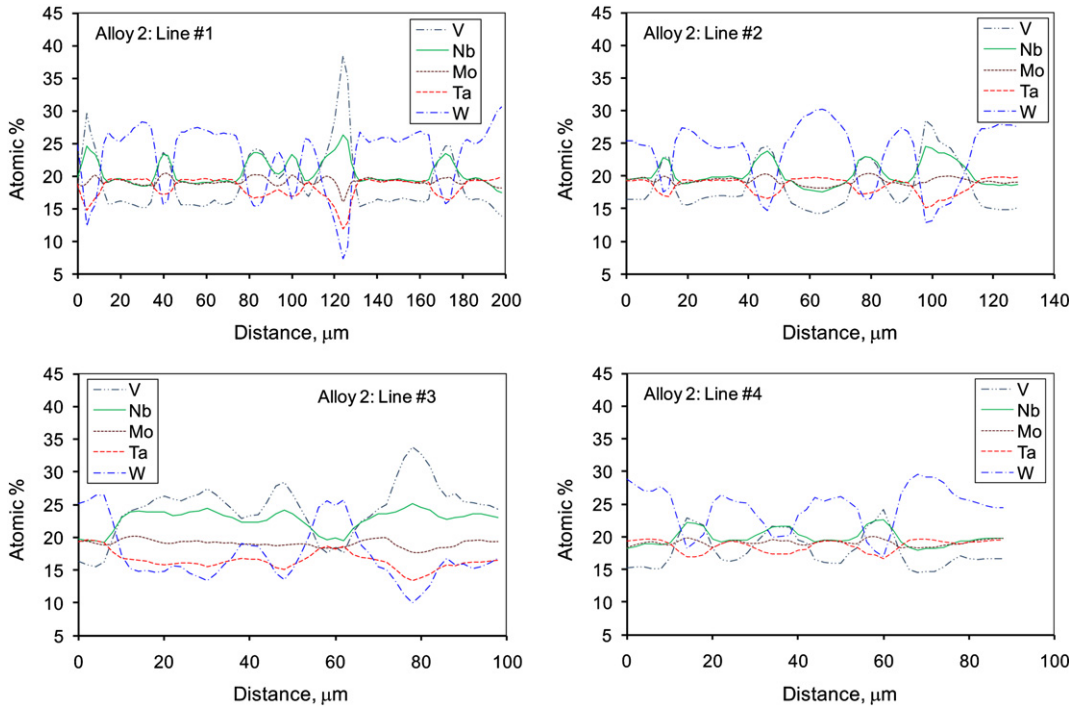


**Fig. 7.** Distribution of elements in Alloy 2 along the lines shown in Fig. 5b.

concentrations in the centers of dendrite arms,  $C_{da}$ , and inter-dendrite regions,  $C_{idr}$ , are also given in these tables. The distribution of elements in the as-cast alloys is non-homogeneous. The level of micro-segregation of the alloying elements is quantitatively described by a partition coefficient  $K = C_{da}/C_{idr}$  [8], which values are given in Tables 3 and 4.

In agreement with the EDS results, the dendrite arms in Alloy 1 are enriched with W and depleted with Nb and Mo, while the interdendritic regions are enriched with Nb and Mo and depleted with W. The concentration of Ta is nearly the same in these regions and is equal to the average concentration (Fig. 6). The addition of V in Alloy 2 not only leads to a finer grain size, but also changes the distribution of other constituents between the dendrite arms and interdendritic regions. For example, W and Ta become more segregated and their concentrations in the interdendritic regions are considerably smaller (by 7.3 and 2.0 at.%, respectively) than the average concentration (Table 4, Fig. 7). In contrast, Mo is distributed more evenly in Alloy 2 than in Alloy 1, while the level of micro-segregation of Nb decreases inside the dendrite arms and increases inside interdendritic regions after addition of V.

**Table 3**

Average,  $C_{aver}$ , minimum,  $C_{min}$ , and maximum,  $C_{max}$ , concentrations of elements in Alloy 1 along four selected lines shown in Fig. 5a. The average concentrations at the centers of dendrite arms,  $C_{da}$ , and inter-dendrite regions,  $C_{idr}$ , as well as comparison of these values with  $C_{aver}$  and the partition coefficient  $K = C_{da}/C_{idr}$  are also given.

Concentrations (at.%)	Nb	Mo	Ta	W
Average, $C_{aver}$	24.8	24.0	24.8	26.4
Minimum, $C_{min}$	20.7	21.7	23.1	18.2
Maximum, $C_{max}$	30.9	27.8	25.6	31.8
$C_{max} - C_{min}$	10.1	6.1	2.4	13.6
Average at the center of dendrite arms, $C_{da}$	22.3	22.3	25.1	30.3
$C_{da} - C_{aver}$	-2.5	-1.7	0.3	3.9
Average in inter-dendrite regions, $C_{idr}$	26.8	25.3	24.6	23.3
$C_{idr} - C_{aver}$	2.0	1.3	-0.2	-3.1
$K = C_{da}/C_{idr}$	0.83	0.88	1.02	1.30

The observed micro-segregation of the constituents is a manifestation of a non-equilibrium solidification of the alloys within the temperature range between the liquidus and solidus temperatures, so that homogeneous distribution of the alloying elements in the growing solid phases is kinetically restricted. The level of the element segregation increases with an expansion of the liquidus–solidus temperature range, which is generally associated with an increase in the difference in the melting temperature of the constituent elements, and an increase in the solidification rate. Because the dendrite arm spacing in Alloy 1 and Alloy 2 is almost the same and there is a direct relationship between the dendrite arm spacing and the solidification rate [9], one can assume that the solidification rate in both alloys was the same. A correlation between excess/deficiency of the concentration of an alloying element in the dendrite arms relative to its average concentration in the alloy,  $\Delta C = C_{da} - C_{aver}$ , and its melting temperature,  $T_m$ , can be found. Enrichment of the dendrite arms, which solidify first, with W is consistent with its high melting temperature,  $T_m$ , relative to the other elements. Nb has the lowest and Mo has the second lowest  $T_m$  among the elements in Alloy 1 (see Table 2), which explains their

**Table 4**

Average,  $C_{aver}$ , minimum,  $C_{min}$ , and maximum,  $C_{max}$ , concentrations of elements in Alloy 2 along four selected lines shown in Fig. 5b. The average concentrations at the centers of dendrite arms,  $C_{da}$ , and inter-dendrite regions,  $C_{idr}$ , as well as comparison of these values with  $C_{aver}$  and the partition coefficient  $K = C_{da}/C_{idr}$  are also given.

Concentrations (at.%)	Nb	Mo	Ta	W	V
Average, $C_{aver}$	20.9	19.1	18.0	22.1	20.0
Minimum, $C_{min}$	17.5	16.0	12.0	7.3	13.9
Maximum, $C_{max}$	26.3	20.4	19.9	30.6	38.5
$C_{max} - C_{min}$	8.8	4.4	8.0	23.3	24.6
Average at the center of dendrite arms, $C_{da}$	19.2	19.0	19.1	26.7	16.0
$C_{da} - C_{aver}$	-1.7	-0.2	1.1	4.7	-4.0
Average in inter-dendrite regions, $C_{idr}$	23.5	19.5	16.0	14.7	26.3
$C_{idr} - C_{aver}$	2.6	0.4	-2.0	-7.3	6.3
$K = C_{da}/C_{idr}$	0.82	0.97	1.19	1.82	0.61

**Table 5**

Vickers microhardness values (in MPa) in ten randomly selected regions of two refractory high-entropy alloys.

Alloy/location	1	2	3	4	5	6	7	8	9	10	Average
W-Nb-Mo-Ta	4547	4398	4332	4418	4547	4537	4626	4379	4256	4507	4455
W-Nb-Mo-Ta-V	4857	5405	5378	5225	5126	5263	5353	5237	5237	5418	5250

preference in interdendritic regions that solidify last. At the same time  $C_{da}$  of Ta, which has an intermediate  $T_m$ , is not much different from its  $C_{aver}$  in Alloy 1. V has the lowest melting point,  $T_m = 1910^\circ\text{C}$ , relative to other alloying elements, and its addition widens the liquidus–solidus range resulting in increasing micro-segregation in Alloy 2 (see Tables 3 and 4).

Fig. 8 shows the dependence of the excess concentration,  $\Delta C = C_{da} - C_{aver}$ , of an alloying element  $i$  (W, Ta, Mo, Nb, or V) inside the dendrite arms in Alloy 1 and Alloy 2 on the difference,  $\Delta T_i = (T_m)_i - T_m^{\text{mix}}$ , between the melting temperature,  $(T_m)_i$ , of this element and a calculated estimate of the melting temperature of an alloy,  $T_m^{\text{mix}}$ . The latter was calculated using the rule of mixtures:

$$T_m^{\text{mix}} = \sum c_i(T_m)_i \quad (4)$$

and is reported for each alloy in Table 2. (Unfortunately, we did not have experimental capability to measure the solidus and liquidus temperatures of these refractory alloys.) It can be seen in Fig. 8 that the segregation of an element  $i$  increases with an increase in  $\Delta T_i$ . This explains why the addition of V increases the micro-segregation of W and Ta while decreasing the micro-segregation of Mo and Nb in Alloy 2. The correlation between  $\Delta C$  and  $\Delta T$  can be described by a linear relationship:

$$C_{da} - C_{aver} = 0.0059(T_m - T_m^{\text{mix}}) \quad (5)$$

where  $\Delta C$  is given in atomic %, and  $\Delta T$  is given in  $^\circ\text{K}$ . For the elements with  $T_m > T_m^{\text{mix}}$ , the partition coefficient  $K > 1$ , while for the elements with  $T_m < T_m^{\text{mix}}$ ,  $K < 1$  (see Tables 4 and 5).

The average concentrations of the elements determined by the EPMA along several lines are slightly different from the values obtained by the ICP-OES analysis (compare Table 1 with Tables 4 and 5). This is evidently due to the micro-segregation and the different volumes of these alloys used in the two methods.

### 3.5. Microhardness

The Vickers microhardness  $H_v$  of both alloys was measured in 10 randomly selected locations and the results are tabulated in Table 5. The average values of  $H_v$  are  $4455 \pm 185$  MPa and  $5250 \pm 281$  MPa for Alloy 1 and Alloy 2, respectively. The higher microhardness in Alloy 2 is either due to a finer grain size or the operation of a non-obvious strengthening mechanism, while the larger scatter is most likely due to stronger element segregation. In addition, V has the smallest atomic radius of the elements in Alloy 2, and this is likely to introduce lattice strains that may also contribute to the higher hardness. Table 2 shows  $H_v$  values for each corresponding BCC alloy constituent at room temperature, which are all much smaller than the  $H_v$  values for the alloys presented in this study. The rule-of-mixtures approach would predict that the hardness of an HEA alloy would obey  $(H_v)_{\text{alloy}} = \sum c_i(H_v)_i$ , giving calculated  $H_v$  values of 1841 MPa and 1596 MPa for Alloy 1 and Alloy 2, respectively (see Table 2). Clearly, the microhardness of these alloys does not follow the rule of mixtures, and moreover, since the grain size difference between these two alloys is relatively small from the perspective of Hall–Petch hardening, the large increase in strength on the addition of V suggests a solid-solution-like hardening mechanism is in effect. Using an approximate relationship between  $H_v$  and the ultimate tensile strength  $\sigma_u$ :  $\sigma_u = H_v/3$ , one can estimate  $\sigma_u = 1485 \pm 62$  MPa for W–Nb–Mo–Ta and  $\sigma_u = 1750 \pm 94$  MPa for W–Nb–Mo–Ta–V.

### 4. Conclusions

Two single-phase refractory high-entropy alloys, W–Nb–Mo–Ta and W–Nb–Mo–Ta–V, were successfully produced by vacuum arc melting. By definition, the alloys had near-equiaxial compositions. Both alloys had a body-centered cubic structure. The lattice parameter, density and microhardness of the W–Nb–Mo–Ta alloy were determined to be  $a = 3.2134(3)\text{\AA}$ ,  $\rho = 13.75 \pm 0.01\text{ g/cc}$  and  $H_v = 4455 \pm 185$  MPa, respectively, while the same properties in the W–Nb–Mo–Ta–V alloy were measured to be  $a = 3.1832(2)\text{\AA}$ ,  $\rho = 12.36 \pm 0.01\text{ g/cc}$  and  $H_v = 5250 \pm 281$  MPa. The lattice parameter and the density of the quaternary alloy followed the rule of mixture of pure elements indicating a fully disordered solid solution. However, the lattice parameter was smaller and the density was slightly larger than those predicted from the rule of mixtures for the quaternary alloy, which was thought to be an indication of some ordering. The Vickers microhardness of the alloys was much higher than that of the pure elements, and contributions from lattice strains and/or a solid-solution-like hardening mechanism are suggested to explain this observation. The alloys had a near-equiaxed dendritic grain structure. The grain size was about  $200\text{ }\mu\text{m}$  and  $80\text{ }\mu\text{m}$  in the quaternary and quinary alloys, respectively, while the thickness of the dendrite arms was about the same in each alloy  $\sim 20\text{--}30\text{ }\mu\text{m}$ . In the quaternary alloy, Ta was uniformly distributed while the dendrite arms were enriched with W and depleted with Mo and Nb. In the quinary alloy, both Ta and Mo were uniformly distributed with slight tendencies for segregation towards the dendrite arms and interdendritic regions, respectively, while the dendrite arms were clearly enriched with W and depleted with Nb and V. The micro-segregation characteristics of the constituents linearly depend on the difference between their melting temperature and the effective

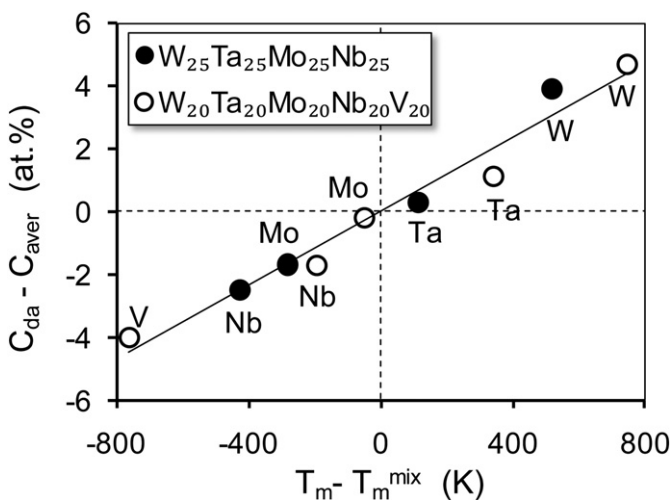


Fig. 8. Dependence of the excess concentration,  $\Delta C = C_{da} - C_{aver}$ , of an alloying element  $i$  (W, Ta, Mo, Nb, or V) inside the dendrite arms in Alloy 1 and Alloy 2 on the difference,  $\Delta T_i = (T_m)_i - T_m^{\text{mix}}$ , between the melting temperature,  $(T_m)_i$ , of this element and the calculated melting temperature of the corresponding alloy,  $T_m^{\text{mix}} = \sum c_i(T_m)_i$ . The data are taken from Tables 2–4. A linear trendline corresponds to Eq. (5).

melting temperature of a corresponding alloy, which is calculated as the average melting temperature of the constituents using Eq. (4).

## Acknowledgements

The authors would like to acknowledge their appreciation of the technical support provided by J.M. Scott, J.M. Shank, F. Meisenkothen, and W.A. Houston (all UES, Inc.) in specimen preparation and characterization. The high-energy X-ray diffraction was performed at the Advanced Photon Source, Argonne National Laboratory. This work was supported by the Air Force Office of Scientific Research (Dr. Joan Fuller, Program Manager) and through USAF Contract No. FA8650-10-D-5226.

## References

- [1] Yeh JW, Chen SK, Lin SJ, Gan JY, Chin TS, Shun TT, et al. *Adv Eng Mater* 2004;6(5):299–303.
- [2] Huang PK, Yeh JW, Shun TT, Chen SK. *Adv Eng Mater* 2004;6(1–2):74–8.
- [3] Yeh JW. *Ann Chim Sci Mat* 2006;31(6):633–48.
- [4] Zhang Y, Zhou YJ, Lin JP, Chen GL, Liaw PK. *Adv Eng Mater* 2008;10(6):534–8.
- [5] Wikipedia, the free encyclopedia. Available from: <http://en.wikipedia.org/wiki/Element>.
- [6] Massalski TB, Okamoto H, Subramanian PR, Kacprzak L. *Binary alloy phase diagrams*. 2nd ed. Materials Park, OH: ASM International; 1990.
- [7] International tables for X-ray crystallography. Birmingham, England; 1968.
- [8] Leo A, Hansch C, Elkins D. *Chem Rev* 1971;71(6):525–616.
- [9] Flemings MC. *Solidification processing*. New York, NY: McGraw Hill, Inc.; 1974.